Tidal heating and the long-term stability of a subsurface ocean on Enceladus

James H. Roberts [*], Francis Nimmo

Department of Earth and Planetary Sciences, University of California at Santa Cruz, 1156 High Street, Santa Cruz, CA 95064-1077, USA

Abstract

Tidal dissipation has been suggested as the heat source for the south polar thermal anomaly on Enceladus. We find that under present-day conditions and assuming Maxwellian behavior, tidal dissipation is negligible in the silicate core. Dissipation may be significant in the ice shell if the shell is decoupled from the silicate core by a subsurface ocean. We have run a series of self-consistent convection and conduction models in 2D axisymmetric and 3D spherical geometry in which we include the spatially-variable tidal heat production. We find that in all cases, the shell removes more heat from the interior than can be produced in the core by radioactive decay, resulting in cooling of the interior and the freezing of any ocean. Under likely conditions, a 40-km thick ocean made of pure water would freeze solid on a ∼30 Ma timescale. An ocean containing other chemical components will have a lower freezing point, but even a water–ammonia eutectic composition will only prolong the freezing, not prevent it. If the eccentricity of Enceladus were higher ($e \geqslant 0.015$) in the past, the increased dissipation in the ice shell may have been sufficient to maintain a liquid layer. We cannot therefore rule out the presence of a transient ocean, as a relic of an earlier era of greater heating. If the eccentricity is periodically pumped up, the ocean may have thickened and thinned on a similar timescale as the orbital evolution, provided the ocean never froze completely. We conclude that the current heat flux of Enceladus and any possible subsurface ocean is not in steady-state, and is the remnant of an epoch of higher eccentricity and tidal dissipation.
© 2007 Elsevier Inc. All rights reserved.

Keywords: Enceladus; Geophysics; Saturn, satellites

1. Introduction

The discovery of the thermal anomaly in the south polar region of Enceladus (Spencer et al., 2006), has launched a great deal of interest in potential activity in the ice shell. 5.8 ± 1.9 GW of heat have been observed pouring out of this region (Spencer et al., 2006), and the global heat flux may be an order of magnitude higher. Such a heat flux was unexpected from a body as small as Enceladus (252 km radius), which under normal circumstances would have cooled very quickly. A likely heat source for the observed thermal anomaly is ongoing internal heating due to tidal dissipation (Matson et al., 2007), an idea first examined by Squyres et al. (1983) and Ross and Schubert (1989) well before this observation. The tidally dissipated energy, $\dot{E}_t$ within a satellite is a strong function of

its orbital frequency ω, eccentricity e, and radius R_s (Segatz et al., 1988)

$$\dot{E}_t = -\frac{21}{2} \text{Im}(k_2) \frac{(\omega R_s)^5}{G} e^2, \tag{1}$$

where G is the gravitational constant, and k_2 is the degree-2 tidal Love number. The dissipation is also a function of the material properties inside the satellite, which are globally described by k_2, and which can be found analytically for a homogeneous body (Ross and Schubert, 1989). For a homogeneous body,

$$k_2 = \frac{3/2}{1 + 19\tilde{\mu}/(2\rho g R_s)}, \tag{2}$$

where ρ is the density, g is the gravitational acceleration, and $\tilde{\mu}$ is the complex rigidity which depends on the rheology.

Enceladus, however, is unlikely to be homogeneous. The tidal dissipation and k_2 depend not only on the material properties of the planet, but the distribution of material as well.

* Corresponding author. Fax: +1 831 459 3074.
 E-mail address: jhr@ucsc.edu (J.H. Roberts).

The thermal anomaly suggests a warm, differentiated interior (Schubert et al., 2007), consisting of a silicate core, overlain by an icy mantle, with a possible ocean separating the two layers (Porco et al., 2006; Nimmo et al., 2007).

The goals of this paper are to determine to what extent tidal dissipation may occur in Enceladus, and how that heat is distributed; to explore how that heat is removed through convection and/or conduction; and to place constraints on the resulting long-term stability and depth of the putative ocean. This paper is organized as follows. We first describe our models for tidal dissipation in multilayered bodies, and present the results of those models applied to Enceladus. In the following sections we present the results of convection and conduction modeling of Enceladus' ice shell including viscoelastic tidal heating. We find that under present-day conditions, tidal heating in the interior of the ice shell and the silicate core is insufficient to prevent an ocean from freezing. Finally, we discuss the implications of those results for the thermal evolution of Enceladus. We suggest that if there is a subsurface ocean on Enceladus today, it cannot be in thermal equilibrium. The current thermal activity is likely a remnant from an epoch of greater heating and higher eccentricity (Meyer and Wisdom, 2007), and the south polar thermal anomaly may be due to a shallow heat source, such as shear heating (Nimmo et al., 2007), rather than volumetric Maxwellian tidal dissipation.

2. Tidal dissipation

Previous studies of tidal dissipation in the Solar System have generally been concerned with the total heat dissipated globally (Kaula, 1964; Zschau, 1978; Segatz et al., 1988; Ross and Schubert, 1989; Ojakangas and Stevenson, 1989; Moore and Schubert, 2000). However, this approach provides no information about the distribution of the tidal heat. In a case like Enceladus, where a great deal of the heat flux is localized, understanding this spatial variation is critically important. Furthermore, when this heat production is coupled with heat transfer (e.g. convection), there is strong feedback between the heating rate at any given location within the satellite and the local temperature and viscosity (Sotin et al., 2002). Because convection is a nonlinear process, using the globally-averaged heating rate may be inappropriate. It is therefore necessary to compute the three-dimensional tidal heating distribution (Tobie et al., 2005) to explore this problem further.

Here, we briefly summarize the procedure used to determine the tidal heat distribution inside a body. Our approach closely follows that outlined in Tobie et al. (2005); details are given below where our procedure departs from theirs. First, we divided the body into material layers. For the purposes of this study, these layers are a small, liquid innermost core (comprising 0.1% of the total volume and required to avoid the singularity at the origin), a silicate core, a liquid water ocean, and an ice shell. The ice shell was further subdivided into a number of smaller layers (20–40 depending on the total thickness), and each layer was assigned a constant density, rigidity, and viscosity.

Second, we solved the equations of motion (Pekeris and Jarosch, 1958; Alterman et al., 1959; Takeuchi and Saito, 1972) by making use of the spherical symmetry assumed in the previous step and separating them into their radial and tangential components. Following a method similar to Alterman et al. (1959) [but a notation more similar to Sabadini and Vermeersen (2004)], the radial functions satisfy six coupled first-order linear differential equations:

$$\frac{dy_1}{dr} = -\frac{2\lambda}{(\lambda+2\mu)r}y_1 + \frac{1}{(\lambda+2\mu)}y_3 + \frac{\lambda\ell(\ell+1)}{(\lambda+2\mu)r}y_2,$$

$$\frac{dy_2}{dr} = -\frac{1}{r}y_1 + \frac{1}{r}y_2 + \frac{1}{\mu}y_4,$$

$$\frac{dy_3}{dr} = \left[-\omega^2\rho r^2 - 4\rho gr + \frac{4\mu(3\lambda+2\mu)}{(\lambda+2\mu)}\right]\frac{1}{r^2}y_1$$
$$- \frac{4\mu}{(\lambda+2\mu)r}y_3$$
$$+ \left[\ell(\ell+1)\rho gr - \frac{2\mu(3\lambda+2\mu)\ell(\ell+1)}{(\lambda+2\mu)}\right]\frac{1}{r^2}y_2$$
$$+ \frac{\ell(\ell+1)}{r}y_4 - \frac{\rho(\ell+1)}{r}y_5 + \rho y_6,$$

$$\frac{dy_4}{dr} = \left[g\rho r - \frac{2\mu(3\lambda+2\mu)}{(\lambda+2\mu)}\right]\frac{1}{r^2}y_1 - \frac{\lambda}{(\lambda+2\mu)r}y_3$$
$$+ \left[-\rho\omega^2 r^2 + \frac{2\mu}{(\lambda+2\mu)}\left(\lambda\left(2\ell^2+2\ell-1\right)\right.\right.$$
$$\left.\left. + 2\mu\left(\ell^2+\ell-1\right)\right)\right]\frac{1}{r^2}y_2 - \frac{3}{r}y_4 + \frac{\rho}{r}y_5,$$

$$\frac{dy_5}{dr} = -4\pi G\rho y_1 - \frac{\ell+1}{r}y_5 + y_6,$$

$$\frac{dy_6}{dr} = -\frac{4\pi G\rho\ell(\ell+1)}{r}y_1 + \frac{4\pi G\rho\ell(\ell+1)}{r}y_2 + \frac{\ell-1}{r}y_6, \quad (3)$$

where y_{1-6} correspond to the radial and tangential displacements, radial and tangential stresses, potential, and potential stress, respectively, μ is the rigidity or shear modulus, λ is the other Lamé parameter, ℓ is the spherical harmonic degree, and r is the radial position. We solved the radial functions [Eq. (3)] using the propagator matrix technique of Sabadini and Vermeersen (2004), subject to the surface boundary conditions appropriate for forced oscillations

$$y_1|_{r=0} = 0, \qquad y_2|_{r=0} = 0, \qquad y_5|_{r=0} = 0,$$
$$y_3|_{r=R_s} = 0, \qquad y_4|_{r=R_s} = 0, \qquad y_6|_{R_s} = -\frac{2\ell+1}{R_s}. \quad (4)$$

More details on this solution method can be found in Appendix A. The appropriate tangential function to use in this case is the tidal potential, Φ (Kaula, 1964), which for small inclinations and to first-order in eccentricity is

$$\Phi = R_s^2\omega^2 e\left[-\frac{3}{2}P_2^0(\cos\theta)\cos\omega t + \frac{1}{4}P_2^2(\cos\theta)\right.$$
$$\left. \times [3\cos\omega t\cos 2\phi + 4\sin\omega t\sin 2\phi]\right] \quad (5)$$

for longitude ϕ and colatitude θ, where P_ℓ^m is the associated Legendre polynomial at spherical harmonic degree ℓ and order m. We computed the radial functions y_i at the midpoint of

Table 1
Tidal heating model parameters

Layer	R_{outer} (km)	ρ (kg m^{-3})	μ (GPa)	η (Pa s)
Core	160	3500	67	10^{17}
Ocean	$R_c \leqslant R_o \leqslant R_{ice}$	1000	0.4	10^4
Ice	$R_o \leqslant R_{ice} \leqslant R_{lith}$	950	4	10^{13}–10^{14}
Lithosphere	250	950	4	10^{19}–10^{20}
e				0.0045
ω				5.308×10^{-5} s^{-1}

Notes. (1) Increasing the core viscosity has no appreciable effect on the ice layer. (2) We treat the ocean as a low-viscosity, low-rigidity layer rather than as an inviscid fluid. This approximation is acceptable as long as τ_M of the ocean is not close to the forcing (orbital) period.

each layer and at the boundaries, and at eight equispaced times over an orbital period. We computed the tidal potential on a regular grid in latitude and longitude, typically $2° \times 2°$.

Third, we determined the strain tensor ε_{ij} at each point on the 3D grid from the displacements (y_1 and y_2), and used the correspondence principle (Biot, 1954) to determine the stress tensor σ_{ij} at each point as well at each time

$$\sigma_{ij} = 2\tilde{\mu}\varepsilon_{ij} + \left[K - \frac{2}{3}\tilde{\mu}\right]\varepsilon_{kk}\delta_{ij}, \qquad (6)$$

where K is the bulk modulus and δ_{ij} is the Kronecker delta. Finally, we compute the heating at each point averaged over the orbital (forcing) period from the complex stress and strain rate (Schubert et al., 2000) and applying the correspondence principle (Biot, 1954):

$$\dot{E}_t = \omega\left[\text{Re}(\sigma_{ij})\,\text{Re}(\dot{\varepsilon}_{ij}) + \text{Im}(\sigma_{ij})\,\text{Im}(\dot{\varepsilon}_{ij})\right]. \qquad (7)$$

3. Tidal heating in Enceladus

Having developed a procedure for calculating the spatially-variable tidal heating in a multilayered, viscoelastic body, we now proceed to apply the results to Enceladus. In this section we carry out simple calculations of tidal dissipation for different prescribed spherically-symmetric internal structures, to assess the likely location and magnitude of tidal heat sources. In reality, of course, lateral variation in the tidal dissipation rate creates similar variations in the interior temperature structure, which in turn affects the viscosity structure. In Section 4 we perturb the local heat production based on the local viscosity values in the convection models. We do not, however, consider lateral variations in material properties when calculating the background heat production rate. Such heterogeneity can be treated numerically (Latychev et al., 2005), but is computationally expensive and beyond the scope of this paper. The global parameters used are summarized in Table 1.

The extent to which heat can be dissipated within the silicate core is important for investigating whether localized seas can be generated due to basal heating of the ice shell (Collins and Goodman, 2007) and whether ammonia can be broken down to form the N$_2$ observed in the plume (Matson et al., 2007). Fig. 1 shows the tidal heating in the Maxwellian core as a function of core viscosity. Only when $\eta_{sil} < 10^{14}$ Pa s does
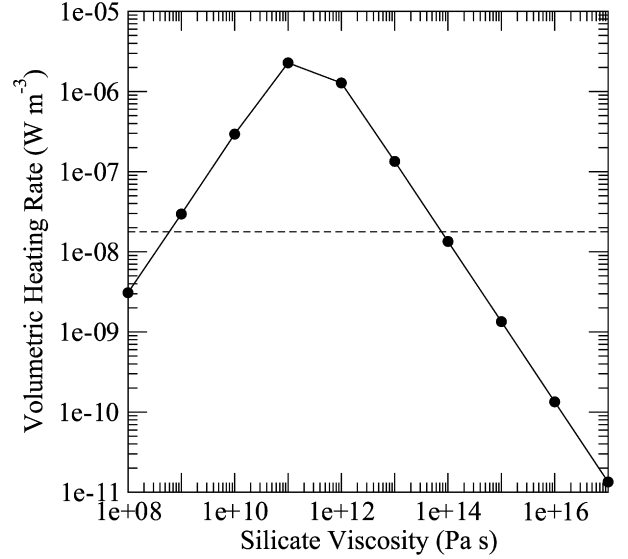

Fig. 1. Tidal heating of the silicate core of Enceladus as a function of viscosity (solid line), compared with present-day radiogenic heating assuming a chondritic composition (dashed line). The core has a density of 3500 kg m^{-3}, radius of 160 km, and a rigidity of 67 GPa. A 20 km thick layer of water and a 70 km thick layer of ice lie atop the core.

the tidal heating (solid line) approach the present-day radiogenic heat ($\sim 1.8 \times 10^{-8}$ W m^{-3}; Multhaup and Spohn, 2007; Schubert et al., 2007) for a chondritic core (dashed line). While a high melt fraction may reduce the viscosity, as is believed to be the case for Io (Scott and Kohlstedt, 2004a), it is not possible to achieve a value as low as 10^{14} Pa s in a silicate material. Experiments on the flow of silicate with high melt fractions indicate that $\eta_{sil} > 10^{15}$ Pa s even if the melt fraction is 0.25, near the critical value for disaggregation (Scott and Kohlstedt, 2004a, 2004b).

The tidal heating in a satellite is a strong function of its size, with the global dissipation increasing as R_s^7, and the volumetric rate as R_s^4, for the case in which $\tilde{\mu}/(\rho g R_s) \gg 1$ [Eqs. (1) and (2)]. Io's radius is more than ten times that of Enceladus' core and thus would be expected to produce over 10^7 times more heat. If we use Io's actual radius and orbital parameters (Murray and Dermott, 1999), and assume that its material properties are the same as our Enceladus model, we find using Eqs. (2) and (1) that Io should dissipate 6×10^6 as much heat as Enceladus' core. The present day surface heat flux at Io is 2.5–3.0 W m^{-2} (Veeder et al., 2004), suggesting that dissipation within the silicate portion of Enceladus should be ~ 0.02 GW, or 1.2×10^{-9} W m^{-3}. Hence, we would not expect significant dissipation in Enceladus' core, even if we assumed an Io-like rheology with a partially molten interior.

Thus, under reasonable rheologic conditions ($\eta_{sil} > 10^{15}$ Pa s), we find it is not possible to generate significant tidal dissipation in the silicate core. We therefore conclude that radioactive decay is the only significant heat source in the silicate layer, producing a total of 0.3 GW. This result is in contrast to the works of Collins and Goodman (2007) and Matson et al. (2007), who assume that $\geqslant 7$ GW of heat is produced in the silicate core.
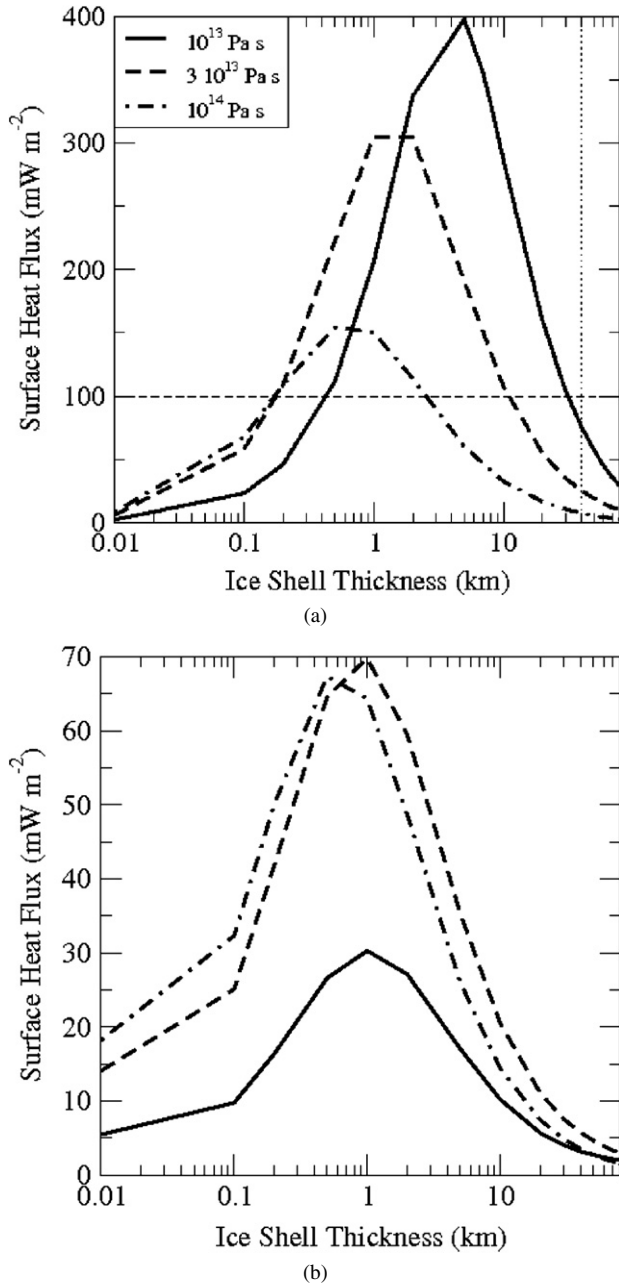
Fig. 2. Surface heat flux predicted from tidal heating models for Enceladus using parameters in Table 1. Horizontal line shows the heat flux measured in the south polar region (Spencer et al., 2006). Vertical line indicates the minimum shell thickness considered for convection models. $\mu = 4$ GPa. For (a), viscosity is constant in the ice shell. For (b), the top half of the ice shell is a high viscosity ($10^6 \times$ the lower layer) lithosphere.

In the absence of an ocean, the ice layer is locked onto the core and the deformation of the former is inhibited by the relative rigidity of the latter. However, substantial tidal heating may be produced in the ice shell if it is decoupled from the core by a subsurface ocean (Moore and Schubert, 2000). Using the methods of Section 2, an ice shell with constant viscosity of 3×10^{13} Pa s, and rigidity of 4 GPa will dissipate only 0.5 GW of heat if it is locked onto the core, but will dissipate 6.4 GW if there is a 500 m ocean between the solid layers. Fig. 2a shows the globally-averaged surface heat flux predicted by these tidal

heating models as a function of ice viscosity η and shell thickness d for a constant viscosity ice shell. A thinner shell is more easily deformable and has a greater tidal heating rate. However, a thin shell also has a smaller volume, limiting the total heat production within it, and thus the total heat flux from the surface. These two competing effects result in a critical shell thickness, d_c at which the maximum heat flow occurs. Although d_c is viscosity-dependent, it is less than 5 km for all the models considered here. d_c is higher for lower-viscosity shells, because the low-viscosity shell is more easily deformable and thus requires a greater thickness to substantially reduce deformation.

The heat fluxes shown in Fig. 2a are for constant-viscosity ice shells. This is intended only to show the effect of the thickness of the ice shell and the ocean on the total heat production, and should not be interpreted to represent the actual viscosity structure. The actual heat flux is probably significantly less than shown in Fig. 2a, because ice viscosity is temperature-dependent (Goldsby and Kohlstedt, 2001), and the ice shell will develop a high viscosity lithosphere that is resistant to tidal deformation. Not only does the lithosphere dissipate very little heat itself, but it impedes the deformation of the deeper layers and reduces the global heating. Fig. 2b shows the heat flux produced by ice shells with a lithosphere equal to half the thickness of the total ice shell. The lithospheric viscosity is 10^6 times that of the lower ice, and the rigidity is the same. The inclusion of the lithosphere strongly reduces the total dissipation. For example, a 40 km thick shell with constant viscosity of 3×10^{13} Pa s will dissipate enough heat to generate 26 mW m^{-2} at the surface (Fig. 2a), but if the viscosity of the top 20 km is raised to 3×10^{19} Pa s, the heat flux drops to 6 mW m^{-2}, a reduction of more than a factor of 4. Since most of the heat is produced near the base of the ice shell and not in the region where the viscosity was increased, this effect occurs because the presence of the lithosphere has reduced the overall shell deformation (and thus k_2). The dissipation rate is a combination of the amplitude of the dissipation and the phase lags (Moore and Schubert, 2000). The phase lag is higher for high viscosity models, but the amplitude is low. When no lithosphere is present (Fig. 2a), the high amplitude in the low viscosity shells yield high dissipations. When a lithosphere is present (Fig. 2b), the deformation is restricted at all depths, but the phase lag in the deep ice is not so affected. Thus the dissipation is more severely reduced for low basal viscosity ($\eta_0 = 10^{13}$ Pa s) models, particularly at low d.

The primary controls on tidal dissipation in our models are the viscosity structure and the thickness of the ice shell (i.e. the depth to the ocean). We have investigated the effects of this tidal heating on the surface heat flux, and the shell thickness by modeling convection and conduction in the ice shell. In the next section (Section 4) we present our convection models, including the tidal heating as a spatially varying internal heat source, for various prescribed basal viscosities and shell thicknesses. This internal heating controls the heat flux at the surface and the bottom of the ice shell. We compare the bottom heat flux to the sub-ice heat provided by radioactive decay in the silicate core, to assess whether or not the interior (and especially the ocean) is cooling or heating (Moore, 2006). In Section 5, we present models of conduction, in which we determine the ice

shell thickness that is consistent with the temperature and heat flux boundary conditions at the base of the ice shell, for a self-consistent ice viscosity structure (cf. Ojakangas and Stevenson, 1989).

4. Convection

Despite the small size of Enceladus, the low viscosity of ice and the large potential for internal heat generation may make convection an efficient process for heat transfer (Barr and McKinnon, 2007). An upwelling diapir may be a good way to generate the localized heat flow in the south polar region (Spencer et al., 2006). Density anomalies and the geoid associated with such an upwelling may also be responsible for an episode of polar reorientation possibly explaining the location of the hotspot (Nimmo and Pappalardo, 2006).

4.1. Modeling

To investigate the behavior of convection under spatially-variable tidal heating, we modeled convection in the ice shell using spherical shell convection models for an incompressible fluid and using the Boussinesq approximation. We used the finite-element convection codes Citcom (Roberts and Zhong, 2004) and CitcomS (Zhong et al., 2000), to which we made a few key modifications discussed below.

Of primary interest to us is the thickness of the ocean beneath the ice shell, therefore our models assume its existence. The ocean decouples the ice shell from the silicate core, so we impose free-slip boundary conditions at the surface and base of the ice shell, and consider convection in the ice shell only. The ice shell is heated both from below by radioactive decay in the core, and from within by tidal dissipation in the ice shell.

The convection is governed by the equations of conservation of mass, momentum and energy:

$$\nabla \cdot \vec{u} = 0,$$
$$-\nabla P + \nabla \cdot \left[\eta \left(\nabla \vec{u} + \nabla^T \vec{u} \right) \right] + \delta \rho g \vec{e}_r = 0,$$
$$\frac{\partial T}{\partial t} + \vec{u} \cdot \nabla T = \kappa \nabla^2 T + H, \tag{8}$$

where $\vec{u}$ is the velocity, P is the pressure, η is the viscosity, T is the temperature, $\delta \rho$ is the density perturbation from the mean density ρ_0, g is the gravitational acceleration, $\vec{e}_r$ is a unit vector in the radial direction, t is time, and κ is the thermal diffusivity. H is the volumetric rate of internal heating; in our case this is the tidal dissipation, and H varies spatially.

At the temperatures and low pressures corresponding to convection within Enceladus' ice shell, Newtonian diffusion creep is likely to dominate (Moore, 2006). We use a temperature-dependent Newtonian rheology for the ice shell

$$\eta = A \exp \left[\frac{E_a}{R_g T} \right], \tag{9}$$

where E_a is the activation energy, and R_g is the gas constant. A is a pre-exponential constant such that at the base of the ice shell, $\eta = \eta_0$, the basal reference viscosity.

We assume the ice shell is in thermal equilibrium with the ocean and the lower boundary is therefore at the melting point of water (273 K). The surface temperature, T_0 is constant in time, but varies with co-latitude, θ due to the variation in insolation (Ojakangas and Stevenson, 1989), such that

$$T_0(\theta) = [\sin \theta]^{1/4} T_{0,\text{eq}}, \quad i < \theta < \pi - i,$$
$$T_0(\theta) = \left[\frac{i^2 + \theta^2}{2} \right]^{1/8} T_{0,\text{eq}}, \quad \theta < i,$$
$$T_0(\theta) = \left[\frac{i^2 + (\pi - \theta)^2}{2} \right]^{1/8} T_{0,\text{eq}}, \quad \theta > \pi - i. \tag{10}$$

$T_0(\theta)$ is normalized to its value at the equator, $T_{0,\text{eq}}$, and i is the inclination of the rotation axis to the orbital plane about the Sun. Note that this is not the same as Enceladus' inclination to its orbit about Saturn, which is very close to zero. Thus, we use Saturn's obliquity of 27° (Murray and Dermott, 1999) for this value.

We use the following nondimensionalizations for the quantities above:

$$s' = \frac{s}{R_s}, \qquad u' = \frac{u}{\kappa / R_s}, \qquad t' = \frac{t}{R_s^2 / \kappa},$$
$$P' = P \frac{\eta_0 \kappa}{R_s^2}, \qquad \eta' = \frac{\eta}{\eta_0}, \qquad T' = \frac{T - T_{0,\text{eq}}}{\Delta T},$$
$$H' = H \frac{R_s^2}{\kappa \rho_0 C \Delta T}, \qquad E' = \frac{E_a}{R_g \Delta T},$$
$$V' = \frac{\rho_0 g R_s V}{R_g \Delta T}, \qquad T_0' = \frac{T_{0,\text{eq}}}{\Delta T}, \tag{11}$$

where all primed quantities are nondimensional. ΔT is the temperature difference across the ice shell at the equator, ρ_0 is the reference density, C is the specific heat, and s represents any length quantity. Note that although T' is 0 on the equator at the surface, the dimensionless surface temperature T_0' is not 0. We use Eq. (11) to nondimensionalize the governing and rheologic equations (8) and (9). Dropping the primes, we obtain

$$\nabla \cdot \vec{u} = 0,$$
$$-\nabla P + \nabla \cdot \left[\eta \left(\nabla \vec{u} + \nabla^T \vec{u} \right) \right] + \text{Ra} \, T \vec{e}_r = 0,$$
$$\frac{\partial T}{\partial t} + \vec{u} \cdot \nabla T = \nabla^2 T + H,$$
$$\eta = \eta_0 \exp \left[\frac{E}{T + T_0} - \frac{E}{1 + T_0} \right]. \tag{12}$$

The vigor of convection is characterized by the dimensionless Rayleigh number, Ra,

$$\text{Ra} = \frac{\rho_0 g \alpha \Delta T R_s^3}{\kappa \eta_0}, \tag{13}$$

where α is the thermal expansivity. Note that we use R_s as the length scale, and not the layer thickness, d. Our Ra will be greater by a factor of $(R_s/d)^3$ from Ra defined in that manner.

For a given set of model parameters, we first ran a tidal heating model for an isoviscous shell ($\eta = \eta_0$) as described in Section 3 to determine a reference heating distribution. We then

set up a corresponding convection model, in which we imported the results of the tidal heating models into Citcom and interpolated them onto the Citcom mesh as a spatially variable internal heating rate. We ran the convection model with temperature-dependent viscosity to a statistical steady-state, and determined the stagnant-lid thickness from the final radial temperature and viscosity profile. We then ran a second tidal heating model in which we included the stagnant lid as a second viscosity layer. The viscosity in the lid was increased by a factor of 10^6 over the deep ice shell. Finally, we ran a second convection model to statistical steady-state based on the new tidal heating.

2D-axisymmetric convection models used a numerical grid of 192 equally spaced elements in latitude, and either 48 or 64 radial elements, refined near the boundaries. Selected models were run in 3D on 12 processors of a PC cluster, using a numerical grid with 1.3 million elements. Details about the 3D grid setup can be found in Zhong et al. (2000).

Our tidal heating models, by necessity, assume constant material properties within each layer. However, lateral temperature and therefore viscosity variations can be quite strong in a convecting system. Furthermore, the two-layer viscosity structure used in the tidal heating models does not fully reflect the radial variations in viscosity due to temperature variations that evolve during convection. To account for these variations, at every timestep of the convection calculations, we perturbed the tidal heating for each element by a factor f (Ojakangas and Stevenson, 1989; Sotin et al., 2002; Han and Showman, 2007)

$$f = \left[\frac{\omega \eta / \mu}{1 + (\omega \eta / \mu)^2} \right] \Big/ \left[\frac{\omega \eta_{\text{ref}} / \mu}{1 + (\omega \eta_{\text{ref}} / \mu)^2} \right] \quad (14)$$

such that $f = 1$ when the local viscosity, η is equal to the reference viscosity η_{ref} for the appropriate viscosity layer in the tidal heating models. For the preliminary tidal heating models with an isoviscous shell, $\eta_{\text{ref}} = \eta_0$. For the tidal heating models with two viscosity layers, $\eta_{\text{ref}} = \eta_0$ in the lower layer, and $\eta_{\text{ref}} = 10^6 \eta_0$ in the upper layer. At each timestep of the convection calculation, the governing equations (12) are solved, and the viscosity for each element is updated according to Eq. (9) based on the current temperature field. The tidal heating assigned to a particular element is the tidal heating predicted from the spherically symmetric tidal heating models described in Section 2, multiplied by f. The advantage to this approach is that for every set of parameters, the heating model need only be computed once rather than at every timestep. Note that the presence of a lithosphere in reducing the global deformation (Figs. 2a and 2b) is taken into account by our procedure.

4.2. Results

Our chief goal is to determine a regime of ice shell thickness d, and reference viscosity η_0, that may be in thermal equilibrium with an ocean, meaning that the basal heat flux F_b across the bottom convective boundary layer in the ice shell is in balance with the heat flux out of the core F_c. Because the radius of the core and the radius of the base of the ice shell are unequal, we must modify F_c by a geometrical factor $n = (R_{\text{core}}/R_{\text{base}})^2$,

Table 2
Convection and conduction model parameters

R_s	250 km
R_b	170–210 km
T_b	273 K
$T_{0,\text{eq}}$	80 K
E_a	60 kJ mol^{-1}
g	0.114 m s^{-2}
k	4 W m^{-1} K^{-1}
α	10^{-4} K^{-1}
κ	1.18×10^{-6} m^2 s^{-1}
ρ_0	950 kg m^{-3}
μ	4 GPa
η_0	10^{13}–10^{14} Pa s
ω	5.308×10^{-5} s^{-1}
i	27°

before comparing it to F_b. If $F_b > nF_c$, then more heat is being extracted from the ocean than is being produced by the core below, and ocean freezing will occur.

We ran several convection calculations exploring the (η_0, d) parameter space. For each model, we first generated a reference tidal heating distribution using the method outlined in Section 2. The reference tidal dissipation was computed on a $2° \times 2°$ regular surface grid at 20–40 points radially (depending on d). For the determination of the reference tidal dissipation, the ice shell consisted of two viscosity layers, a lower layer at η_0, and a lithosphere at $10^6 \times \eta_0$. The thickness of the lithosphere varied based on d and η_0, and was computed as described above from the results of an initial convection model in which the tidal heat assumed an isoviscous shell. The model parameters are summarized in Table 2.

An example of the initial heating distribution, averaged about the rotation axis is shown in Fig. 3a, with $d = 70$ km and $\eta_0 = 3 \times 10^{13}$ Pa s. Note that the heating is greatest near the base of the ice shell and especially at the polar regions. In the lithospheric layer, the heating is insignificant (but we include it in the convection models). The reference heating value was interpolated onto the Citcom grid, and the corresponding convection model was run. In the convection calculation, the lithosphere developed self-consistently through the rheologic equation (9), and the tidal heating was computed at each timestep based on the local viscosity [Eq. (14)]. The steady-state lithospheric thickness was then used to recompute the background tidal dissipation which was then used as the starting point for the subsequent convection model. Each calculation was run until the heat flux reached a statistical steady-state. The final heat distribution (Fig. 3b) is not dramatically different from the initial, but does reflect the convective structure with pronounced downwellings and weaker upwellings. Because the basal temperature is fixed, the basal heat flux depends on the interior temperature, which in turn depends upon the heat distribution in the ice shell. Fig. 3c shows the final radial temperature profile for the case in Fig. 3b. The ice shell in this case has a very thick stagnant lid in which heat production is insignificant. This lid insulates the interior very effectively, raising the interior temperature to near the melting point. There is, however, a thin lower boundary layer, across which $F_b = 22$ mW m^{-2}.
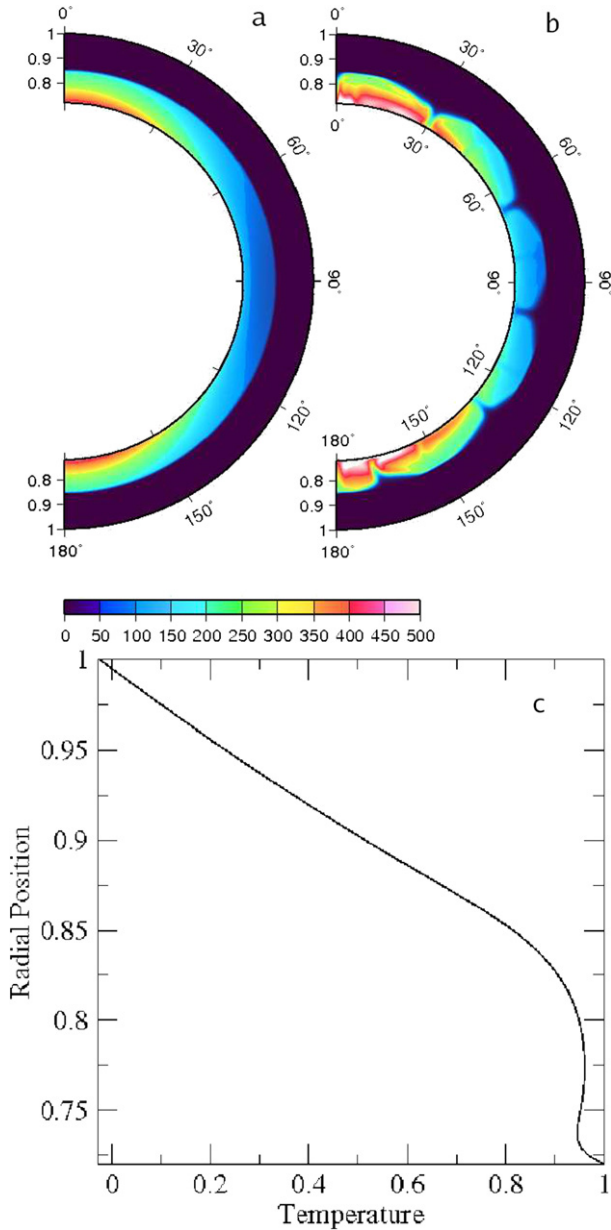
Fig. 3. Initial (a) and final (b) heating distributions for an axisymmetric convection model with a 70 km thick ice shell above a 20 km ocean with basal viscosity 3×10^{13} Pa s, and a lithospheric thickness of 38 km. The heating rates shown are in terms of 10^{-9} W m^{-3}. (c) Radial temperature profile for the case shown in (b). Tidal dissipation in the interior generates heat in the deep part of the ice shell, heating this region almost to the melting point. A thick (40 km) stagnant lid insulates the lower region. The basal heat flux in this case is 22 mW m^{-2}, and the surface heat flux is 15 mW m^{-3}, for a global total of 9.0 and 11.8 GW at the base and surface, respectively.

For this particular model, despite the high interior temperature, F_b is still far in excess of the chondritic value of nF_c (0.75 mW m^{-2} at $R_b = 180$ km, which corresponds to $\dot{E} = 0.3$ GW in the core), suggesting that either a thicker shell or greater internal heating is required for long-term equilibrium. We ran a total of 11 cases to determine the effect of d and η_0 on the heat flow balance. Fig. 4 summarizes the results for the heat flow from the 2D axisymmetric convection models.
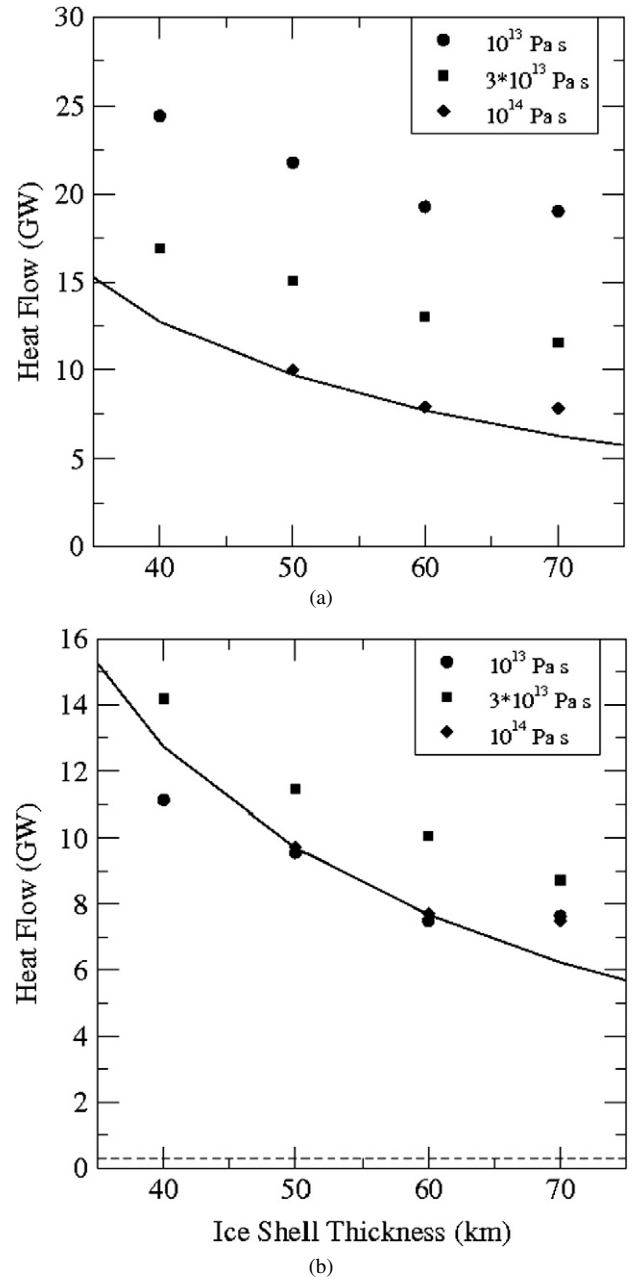

Fig. 4. Global heat flow across the surface (a) and base of the ice shell (b) for convection models. Solid line represents the conductive heat flow. Dashed line is the heat generated by radioactive decay in the silicate core. Note in (b) that some cases with $\eta_0 = 10^{13}$ Pa s have *lower* heat flow than would be removed conductively. These models are so warm that melting is widespread.

In general we found that the heat flow at both boundaries increased with increasing Ra (i.e. with decreasing viscosity) and with decreasing shell thickness (Fig. 4). Note that the high reference viscosity (10^{14} Pa s) models are essentially conductive if the shell is thinner than 70 km. Note also, that while the low viscosity (10^{13} Pa s) models have the highest surface heat flows, their basal heat flows are similar to those for the high reference viscosity cases, and in some cases are below the conductive value. The low reference viscosity shells have substantially more heat to remove. Although they convect more vigorously, these weaker shells have very warm interiors (al-

though still below the melting point), and are thus inefficient at cooling the core. Nevertheless, in every case far more heat is drawn across the base of the ice shell than can be generated by radioactive decay in the core (dashed line in Fig. 4b), implying a rapid cooling of the ocean and interior. This key result will be discussed in more detail in Section 6.

5. Conduction

We have also considered the possibility that the ice shell may be conductive. This is certainly the case if the ice shell is thin ($\lesssim$40 km), or if the ice reference viscosity is relatively high ($\gtrsim 10^{14}$ Pa s).

5.1. Modeling

Our goal is to determine what conductive ice shell thickness d will be in thermal equilibrium with a liquid ocean beneath it. Thermal equilibrium requires not only that the base of the ice shell be at the same temperature as the ocean, but also that the heat flow across the base of the ice shell is equal to the radiogenic heat produced in the silicate core. That is, we attempt to find a shell thickness in which heat production and heat loss are in balance, resulting in no net heating or cooling of the interior, and thus no freezing of the ocean or melting of the ice shell.

Unlike a convective system, the interior of a conductive ice shell is far from isothermal. The strong radial temperature variation throughout the ice shell leads to strong viscosity variations. Our tidal heating model requires constant viscosity within a layer, therefore we break the ice shell into an onion-skin model of 2-km thick layers. We make an initial guess as to the thickness and radial viscosity structure of the ice shell and calculate the tidal dissipation, $H_T(r, \theta)$. In steady state, the conductive temperature within the ice shell satisfies:

$$k\nabla^2 T + H_T(r, \theta) = 0, \tag{15}$$

where k is the thermal conductivity. We then determine the 2D-axisymmetric conductive temperature profile subject to this heating and to the same temperature boundary conditions as in the convection case. The bottom of the shell is at 273 K (melting point of water), and the equatorial surface temperature is 80 K, and varies with latitude according to Eq. (10). We then recompute the viscosity based on this conductive temperature profile, according to Eq. (9). If the ice shell is in thermal equilibrium, then the heat flow across the base of the ice shell should match the heat flow produced by the core. The basal and core heat fluxes (F_b and F_c, respectively) are

$$F_b = -k \int_0^\pi \frac{dT}{dr} \, d\theta, \qquad F_c = \frac{1}{3} \overline{H_{\text{core}}} R_c. \tag{16}$$

Because F_c comes from radioactive decay in the core, we assume that it does not vary with position. Based on a present-day chondritic heating rate, $F_c = 0.95$ mW m^2 at R_{core}. If nF_c does not equal F_b, we adjust the thickness of the ice shell d, and calculate the tidal heating for the new d and η profile. We iterate between the tidal heating and conduction models until either
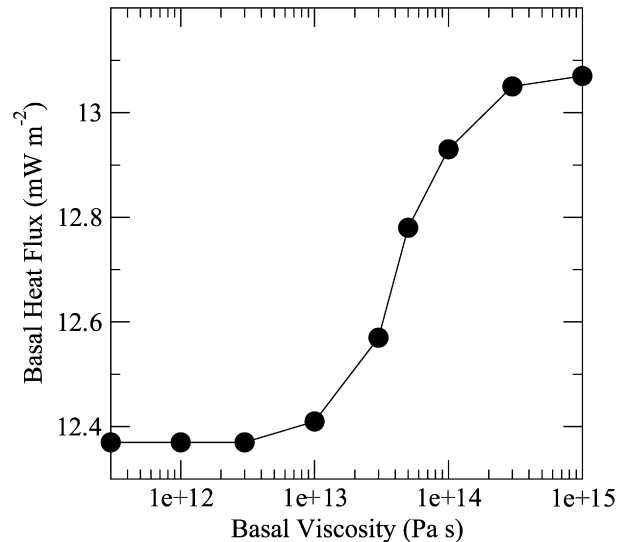

Fig. 5. Minimum F_b for a 90 km conductive ice shell as a function of the basal viscosity. That is, the ice shell is as thick as possible. The viscosity in the shell is temperature dependent with $E_a = 60$ kJ/mol and the tidal heating is calculated accordingly. In all cases, F_b exceeds F_c from radioactive decay (0.95 mW m^{-2}) in the core.

$|F_b - nF_c| \leqslant 0.001$, the shell melts completely, or the ocean freezes completely.

5.2. Results

Given Enceladus' current orbital parameters, we find that the ocean beneath a conductive ice shell freezes completely, that is $F_b > nF_c$ for all reference viscosities considered for the ice shell (10^{13}–10^{14} Pa s). Fig. 5 shows the minimum F_b for a conductive shell over an ocean, that is the F_b when the shell is 90 km thick, and for a constant $k = 4$ W m^{-1} K^{-1}. Clearly, the basal heat flux greatly exceeds the expected radiogenic heat flux.

These results assume that the current orbital parameters are in a steady state. The Saturn system, however, is very complex dynamically. One might imagine that through interactions with other satellites, Enceladus' eccentricity may have been higher in the past (Meyer and Wisdom, 2007). If $e \geqslant 0.0156$ (roughly 3.3 times the present value), the heating in the ice shell is sufficient to reduce F_b below nF_c, and would permit a liquid ocean to persist long-term between the silicate core and the ice shell. We show as an example the radial temperature profile and heat distribution for a 70-km thick conductive ice shell in thermal equilibrium (Fig. 6), in which we have used a higher eccentricity ($e = 0.0156$) than the current one. The heating is very sensitive to the temperature (and viscosity), and is only strong near the bottom where the ice is warm.

6. Discussion

6.1. Lifetime of the ocean

In both the tidally-heated convective and conductive cases, we find that heat is removed from the ocean of Enceladus faster
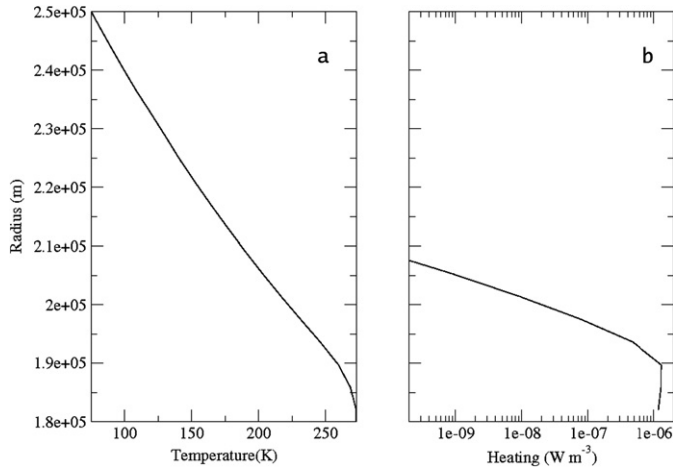
Fig. 6. Radial temperature and heat distributions for a 70-km thick conductive ice shell in thermal equilibrium with $\eta_0 = 3 \times 10^{13}$ Pa s. The heating is concentrated in the warmer, less viscous part of the ice shell and drops off dramatically when $T < 200$ K. Heating is negligible in the upper half of the ice shell. $F_b = 0.95$ mW m^{-2} (the expected value from radiogenic core heating), and $e = 0.0156$, exceeding the present-day value by a factor of ~ 3.5.
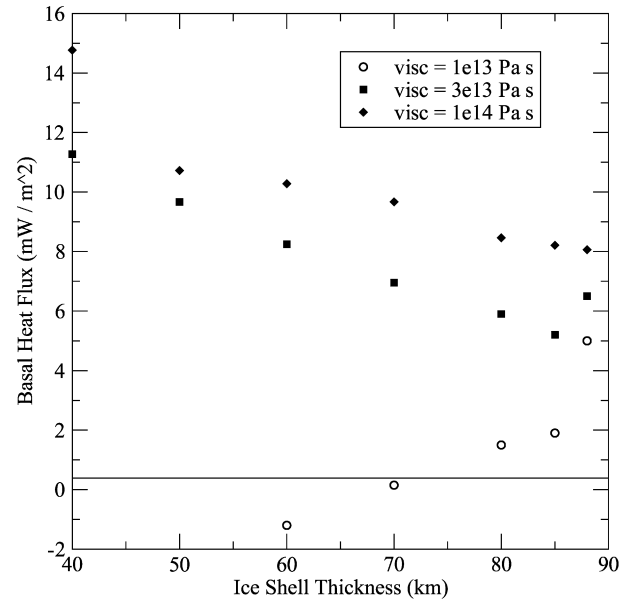

Fig. 7. Heat flux across the base of the ice shell for convection models with no lithosphere. Solid line is the heat generated by radioactive decay in the silicate core. All values have been normalized to the surface area of Enceladus. Compare with Fig. 4. F_b for $\eta_0 = 10^{14}$ Pa s is very similar to the lithospheric version, for $\eta_0 = 3 \times 10^{13}$ Pa s F_b is slightly reduced. F_b for $\eta_0 = 10^{13}$ Pa s is greatly reduced, and even negative in some cases, indicating the ice is warmer than the underlying ocean and is melting.

than it is generated by radioactive decay in the silicate core. A large amount of interior cooling (7–25 mW m^{-2}) occurs, resulting in the freezing of the ocean onto the base of the ice shell. A thicker ice shell resists deformation to a greater degree and is less strongly heated (Fig. 4b), accelerating the freezing of the ocean. Once the ocean freezes entirely, the ice shell is mechanically coupled to the silicate core, severely reducing the tidal dissipation in the ice. If Enceladus enters this state, it will likely remain frozen indefinitely, barring an external heat source delivered to the interior. The timescale for the freezing of the ocean depends upon the initial thickness of the ocean, but a 40 km thick ocean with $(F_b - nF_c) = 8$ mW m^{-2} will freeze in ~ 30 Ma.

We have identified four ways in which the lifetime of the ocean may be extended. The first is to have greater heat production in the core, thereby increasing F_c. However, it is not obvious how this would be accomplished. The composition of the core is poorly known, but it is unlikely to be so different from chondritic that the radioactive heat production rate is substantially greater. Tidal dissipation in the core is negligible at any plausible silicate viscosity, assuming the core behaves in a Maxwellian manner; the core radius is simply too small. The core might behave in some non-Maxwellian manner that is more dissipative, but no such mechanism has been proposed. Unlike for larger planets such as Earth or Mars, secular cooling of the core is unlikely to be a significant source of heat today, because the diffusion time for Enceladus is less than 2 Ga.

The second way to prolong the ocean is to increase the heating in the ice shell, thereby reducing F_b. Eliminating the lithosphere in the tidal dissipation models for convective shells increases the global heating by a factor of several (compare Figs. 2a and 2b). Fig. 7 shows the convective basal heat flux for the preliminary runs of all the cases shown in Fig. 4, that is without the lithosphere. In this situation, the low-viscosity (10^{13}) ice shells have sufficiently low F_b to prevent the freezing of the ocean. However, these cases also have widespread

overheating and melting of the ice shell. These ice shells will therefore thin, become heated even more, and experience runaway melting until they become conductive. At this point the heating will drop off and the shell will begin to thicken again. One might envision a situation in which the ice shell oscillates between a thick, convective, melting shell, and a thin, conductive, freezing one. However, this scenario depends on the assumption that convection can take place without a rigid, near-surface layer developing, which contradicts the general experience of strongly temperature-dependent convection (e.g. Solomatov, 1995).

A third possibility for maintaining a liquid ocean is if the liquid is not be pure water. If the ocean contains substantial amounts of other volatiles (e.g. ammonia), the melting point may be severely depressed. We have tested this by running additional conduction models as in Section 5 in which we lowered the basal temperature. However, even at the H_2O–NH_3 peritectic temperature of 175 K (Leliwa-Kopystyński et al., 2002), the conductive $F_b \sim 6$ mW m^2, which is still in excess of nF_c. This result is not unexpected: we have essentially reduced the temperature contrast by half, and thus reduced the heat flux by the same fraction. This is not sufficient to prevent freezing, although it will slow it down. Furthermore, there is currently no observational evidence for NH_3 in the plumes (Waite et al., 2006). Therefore, while chemical effects may play an important role in the ocean and ice shell of Enceladus, they cannot alone prevent the freezing of the ocean.

As a fourth possibility, we note that sufficiently low thermal conductivity due to near-surface porosity may slow the heat loss from the interior below our estimates. However $k <$

$0.5\ \mathrm{W\,m^{-1}\,K^{-1}}$ is required to satisfy the condition on F_b, an unrealistically low value.

Studies of orbital dynamics suggest that the current observed heat flux cannot be sustained in the steady state, independent of the material properties of Enceladus (Meyer and Wisdom, 2007). If we relax the assumption that Enceladus is in the steady-state, the apparent transient nature of a subsurface ocean becomes easier to understand. The global tidal dissipation is a strong function of eccentricity [Eq. (1)]. If e were higher in the past, the global tidal dissipation would also have been higher. A transient ocean could exist beneath the ice shell today as a remnant of an earlier epoch of higher heating. If Enceladus' eccentricity is periodically pumped up, then the ocean could be periodically thickened, provided that it never freezes completely. The timescale for orbital evolution is on the order of tens of Ma, similar to the freezing timescale indicated above.

6.2. True polar wander

True polar wander (TPW) due to buoyant upwellings in the ice shell have been proposed as an explanation for the south polar location of the observed hotspot (Nimmo and Pappalardo, 2006). If the lithosphere is sufficiently strong (likely for $T_s \sim 80\ \mathrm{K}$), the plume buoyancy is not compensated by dynamic topography at the surface. The net negative mass anomaly can cause poleward TPW if the load can overcome the fossil rotational bulge (Willemann, 1984). Large amounts of reorientation are achieved if the nondimensional load, $Q \gtrsim 1$ (Willemann, 1984), where

$$Q = \frac{3\sqrt{5}\,g N_{20}}{(R_s \omega)^2 (k_2^* - k_2)}, \tag{17}$$

where N_{20} is the geoid at degree-2 and k_2^* is the fluid love number. For the Enceladus models studies here, k_2 is typically of order 0.01 vs 0.75 for k_2^*. The $\ell = 2$ geoid due to internal loads (Zhang and Christensen, 1993) is

$$N_{20}(R_s) = \frac{3}{5} \int\limits_{r_i}^{R_s} \left(\frac{r}{R_s}\right)^4 \frac{\delta\rho(r)}{\bar{\rho}}\,\mathrm{d}r. \tag{18}$$

For a 40 km tall upwelling in the lower half of the ice shell, a density reduction of about 1.75% in the buoyant upwelling is required for $Q = 1$. If the density contrast arises purely through temperature variations, a lateral variation of 175 K is required. This variation is not supported by our models. However, localized partial melting near the base of the ice shell could remove impurities, enhancing the density contrast between the clean ice in the upwelling and the dirty ice of the surroundings (Nimmo and Pappalardo, 2006). Such thermochemical modeling is beyond the scope of this paper. Furthermore, although the heating pattern is $\ell = 2$, this is not reflected very strongly in the temperature profiles, which are dominated by $\ell = 8$ (Fig. 3). Effects besides the tidal dissipation may be required to explain the south polar thermal anomaly.

6.3. Spatial pattern

Also of interest is the spatial pattern of tidal heating and the surface heat flux, which may be indicative of the pattern of convection in the underlying material. The observed thermal anomaly (Spencer et al., 2006) is a single large scale feature, dominated by spherical harmonic degree $\ell = 1$. If the hotspot is the surface expression of convection in the ice shell, then it suggests that the convection is at the same wavelength. Czechowski and Leliwa-Kopystyński (2005) have noted the correlation between spatial patterns of tidal heating and flow patterns, although they do not consider the feedback of the convection on the tidal heating pattern. However, developing a long-wavelength convective pattern is not easy. Degree-1 convection has been successfully modeled for the Earth (McNamara and Zhong, 2005) and Mars (Harder and Christensen, 1996; Breuer et al., 1997; Harder, 2000; Roberts and Zhong, 2006). However, those models made use of mobile lids, phase transitions, and/or strong radial viscosity variations, all of which help to increase the wavelength of convection, and none of which are applicable to Enceladus. Furthermore, Enceladus has some additional characteristics that serve to reduce the wavelength. The core is proportionally much larger on Enceladus ($R_c = 0.64 R_s$) than on Earth or Mars, resulting in a much thinner convective region. The dominant heat source in the ice shell of Enceladus is tidal dissipation, and the tidal potential is entirely an $\ell = 2$ function (Kaula, 1964). It is not clear how an $\ell = 1$ pattern may arise from a $\ell = 2$ forcing. To study this problem, we ran some of the convection cases from Section 4 in 3D. Fig. 8 shows the residual temperature and the spherical harmonic decomposition for temperature structures for the same parameters as the axisymmetric case shown in Fig. 3. The convection planform is characterized by a large number ($\sim$30) of small-scale upwellings, superimposed upon a $\ell = 2$ background (Fig. 8a), rather than a single long-wavelength upwelling that might explain the south polar hotspot. The spectrum of temperature structures also shows no significant power at $\ell = 1$; it is one of the weakest wavelengths (Fig. 8b). Hence, our current models cannot explain the predominately $\ell = 1$ thermal anomaly observed; this is an area of active investigation.

6.4. Alternate rheologies and heating mechanisms

The choice of rheology in the tidal heating models may affect the amount of energy dissipated in the body. Following Sabadini and Vermeersen (2004) and Tobie et al. (2005), we have treated Enceladus as a Maxwellian viscoelastic solid [see Eq. (6)], because this rheology matches the real response of planetary materials in both high frequency ($\omega \gg 1/\tau_M$) and low frequency ($\omega \ll 1/\tau_M$) limits (Ross and Schubert, 1986). By comparison, the Kelvin–Voigt rheological model does not reproduce the real behavior in either limit.

It is conventional to consider the steady-state (secondary) creep of ice when calculating tidal heating. However, tidal strains are low and timescales are short, in which case the transient (initial or primary) creep of ice may play a role (e.g. Sinha, 1978). For primary creep, the strain goes as $\sigma^a t^b$ where σ is
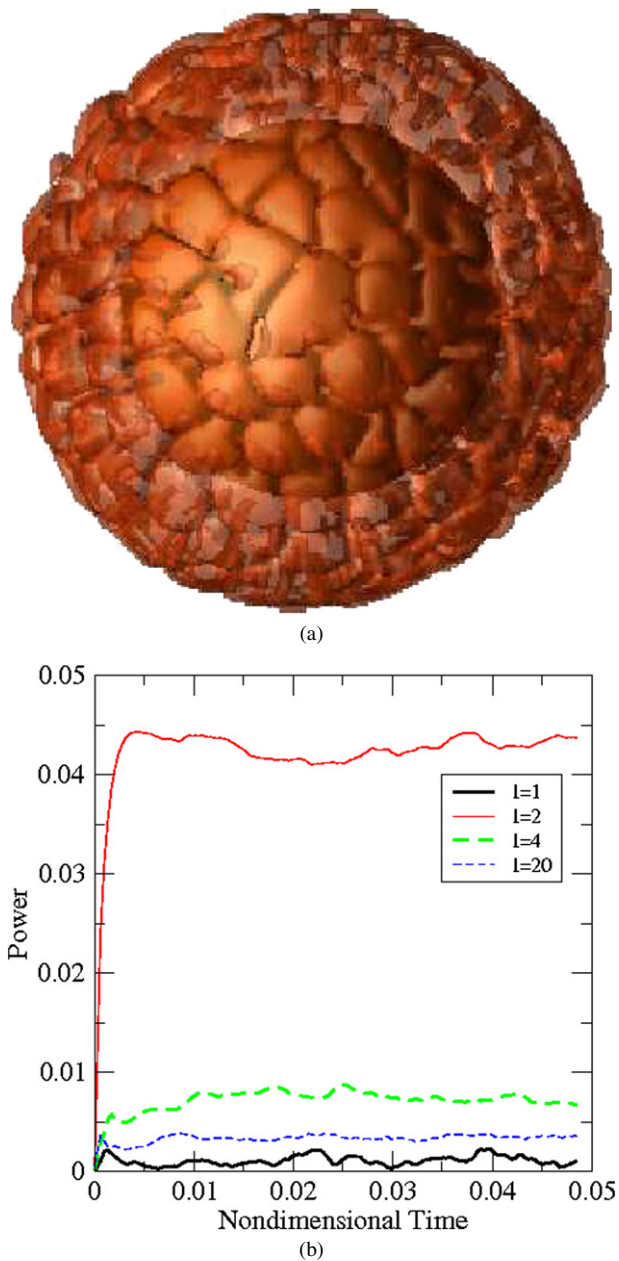
(a)

(b)

Fig. 8. (a) Isosurface of temperature for a 3D convection model with tidal heating. $Ra = 9.2 \times 10^8$, $E_a = 60$ kJ/mol. The isosurface is for $T' = 0.95$. (b) Spectrum of temperature structures for the case in (a) at $\ell = 1$ and at the three strongest harmonics. There is no indication in this, or other 3D models of a single long-wavelength upwelling that might explain the south polar thermal anomaly (Spencer et al., 2006).

stress, and a and b are constants. Integrating over a tidal cycle of period T_T, the effective viscosity of the ice (= stress/strain rate) is given by

$$\eta_{\text{eff}} = \sigma^{1-a} T_T^{1-b} c^{-1}$$

$$= 2.5 \times 10^{12} \left(\frac{0.1 \text{ MPa}}{\sigma} \right)^{1.43} \left(\frac{T_T}{10^5 \text{ s}} \right)^{1/3} \text{Pa s}, \qquad (19)$$

where c is a (temperature-dependent) constant and the numerical values are taken from Azizi (1989) for ice at 268 K.

This effective viscosity is somewhat lower than the range of steady-state reference viscosities assumed, suggesting that primary creep may play a non-negligible role. The effective modulus of ice is also slightly frequency-dependent (Sinha, 1978), but the total variation is a factor of ≈ 2 and is thus unlikely to change our results.

In this paper, we have not considered the effects of non-Maxwellian heating mechanisms on the tidal dissipation. One such possibility is tidally-driven shear heating along the tiger stripes, that may help explain the pattern of heat flux as well as the amplitude (Nimmo et al., 2007). This localized near surface heating can also affect the deeper convection (Roberts and Nimmo, submitted for publication), although how the near-surface heating is initiated remains an open question.

We have only considered a fully differentiated Enceladus (Schubert et al., 2007). However, it may be that Enceladus is only partially differentiated, and the interior similar to Callisto (Nagel et al., 2004; McKinnon, 2006), where an ocean may still be present (Zimmer et al., 2000). In this case, the ice–silicate mantle will have a higher rigidity and viscosity than pure ice, substantially reducing the tidal dissipation. Such a body would probably be conductive rather than convective. We expect the former effect would promote the cooling of the interior and cause the ocean to freeze more rapidly.

6.5. Summary

To summarize our results, we find that a liquid ocean cannot exist in thermal equilibrium beneath the ice shell of Enceladus, for either convective or conductive ice shells. Heat transport across the ice shell is simply too efficient compared with the small amount of radiogenic heat generated in the silicate core. This conclusion is supported by independent dynamical arguments (Meyer and Wisdom, 2007), which suggest that the observed heat anomaly (Spencer et al., 2006) cannot be sustained, given Enceladus' current eccentricity. Our results do not preclude the existence of a transient ocean, left over from a period of higher heating, due to higher eccentricity. Some of the models shown here are able to replicate the 3–7 GW observed by Spencer et al. (2006) for the south pole, but the models cannot reproduce the spatial pattern. Future work in this area may consider the effects of alternate heating mechanisms, such as shear heating (Nimmo et al., 2007), and the effects of chemical heterogeneity on the convective planform and thermal evolution of Enceladus.

Acknowledgments

Appendix A. Solution method for tidal dissipation radial functions

In our method of solving for the tidal dissipation within Enceladus described in Section 2, we have generally followed
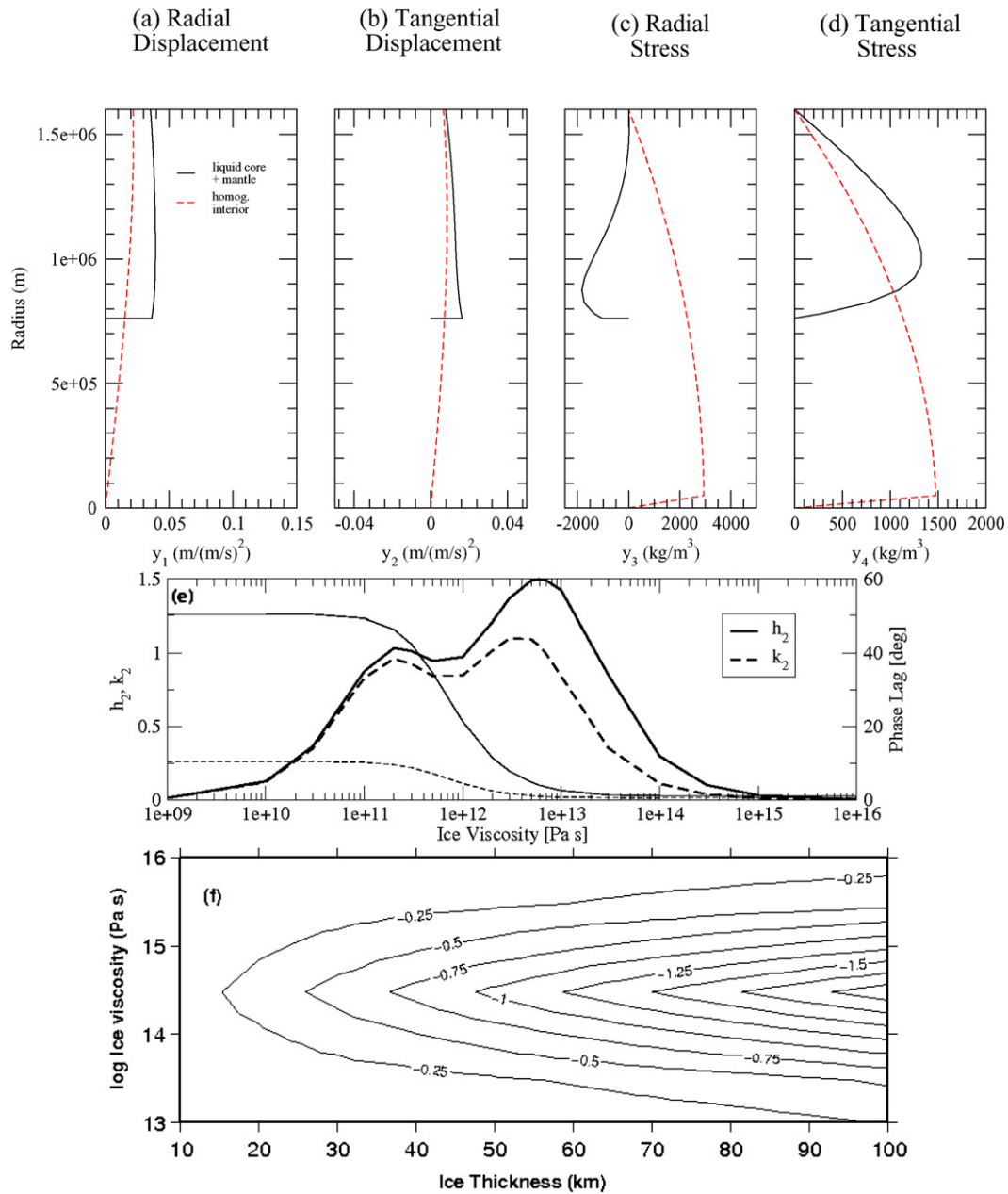
Fig. 9. Results for benchmarking the tidal dissipation code. (a–d) Radial functions for a homogeneous body (dashed lines), and for a layered body composed of a silicate mantle (solid lines) overlying an iron core, using parameters from Tobie et al. (2005), and equivalent to their Fig. 2. For the layered model, results are only shown for the silicate portion. (e) Plot of Love numbers (thin lines) and phase lags (bold lines) vs ice viscosity for the Europa model of Moore and Schubert (2000). Comparable to their Fig. 2. Note that the Love numbers are for the case with no lithosphere, and the double-peaked phase lags are for the case with a lithosphere. (f) Phase lag of h_2 as a function of shell thickness and ice viscosity for the Europa model (Moore and Schubert, 2000) with an ocean. Comparable to their Fig. 3.

a method similar to that outlined by Tobie et al. (2005), the details for which come from earlier works on free oscillations motivated by terrestrial seismological problems (Pekeris and Jarosch, 1958; Alterman et al., 1959; Takeuchi and Saito, 1972) and are not repeated here in greater detail than the summary in Section 2. However, our solution method differs from Tobie et al. (2005) in one key respect: we do not use a numerical shooting method to solve for the radial functions, but an analytical propagator-matrix approach based on Sabadini and Vermeersen (2004), which we describe here.

The radial functions, y_i satisfy a set of six first-order linear equations [Eq. (3)] and six boundary conditions [Eq. (4)]. Pekeris and Jarosch (1958) give an analytical solution for a homogeneous body. Enceladus is probably differentiated (Schubert et al., 2007) and its material properties vary substantially with radius. An analytical solution is impossible for a fully variable body. However, if we treat Enceladus as a set of spherically-symmetric "onion-skin" layers, we can use a propagator matrix (Sabadini and Vermeersen, 2004) technique to solve for the y_i, assuming that the material properties (μ, λ, ρ)

are constant within each layer. For a given layer k, we can express the solution vector $\vec{y}^{(k)} = y_i^{(k)}$ in terms of the fundamental matrix Y and a vector integration constant $\vec{C}^{(k)}$ that describes the internal boundary conditions for that layer (Sabadini and Vermeersen, 2004).

$$\vec{y}^{(k+1)}|_{r_k} = Y^{(k+1)}|_{r_k} \vec{C}. \tag{A.1}$$

Y and its inverse are 6×6 matrices and are defined by Sabadini and Vermeersen (2004). There is no need to explicitly find $\vec{C}$ for each layer. The internal boundary conditions they represent arise from the fact that y_i must be continuous across each layer interface

$$y_i^{(k+1)}|_{r_k} = y_i^{(k)}|_{r_k}, \tag{A.2}$$

where r_k is the radius of the interface between layer k and layer $k + 1$ above. We can express the $\vec{C}$ for one layer in terms of the other:

$$Y^{(k+1)}|_{r_k} \vec{C}^{(k+1)} = Y^{(k)}|_{r_k} \vec{C}^{(k)},$$
$$\vec{C}^{(k+1)} = \left[Y^{(k+1)}\right]^{-1}|_{r_k} Y^{(k)}|_{r_k} \vec{C}^{(k)} \tag{A.3}$$

and therefore at any point in layer $k + 1$

$$\vec{y}^{(k+1)}(r) = Y^{(k+1)}(r)\left[Y^{(k+1)}\right]^{-1}|_{r_k} Y^{(k)}|_{r_k} \vec{C}^{(k)}. \tag{A.4}$$

We do this for all N layers in the body (where $k = 0$ is the innermost core, and $k = N - 1$ is the top layer), so that at the surface:

$$\vec{y}|_{R_s} = \left(\prod_{k=N-1}^{1} Y^{(k)}|_{r_k}\left[Y^{(k)}\right]^{-1}|_{r_{k-1}}\right) Y^{(0)}(r_0)\vec{C}^{(0)} \tag{A.5}$$

and $\vec{y}$ everywhere is based on the $\vec{C}$ of the lowest layer, with radius r_0, the innermost core. The conditions at $r = r_0$ can be expressed as an interface matrix I_0 as

$$Y^{(1)}(r_0)\vec{C}^{(1)} = I_0\vec{C}_0. \tag{A.6}$$

Three boundary conditions are specified at the center of the body [Eq. (4)], thus reducing I_0 to only a 6×3 matrix and $\vec{C}_0$ to a three component vector. $\vec{C}_0$ is found from the surface boundary conditions, after substituting Eq. (A.6) into (A.5),

$$\vec{y}|_{R_s} = \left(\prod_{k=N-1}^{0} Y^{(k)}(r)\left[Y^{(k-1)}\right]^{-1}|_{r_k}\right) I_0(r_0)\vec{C}_0. \tag{A.7}$$

This permits us to solve for the radial functions y_i at all points in layers $k = 1$ to $N - 1$. Note that this approach requires the presence of a fluid innermost core of radius r_0 as layer $k = 0$ inside of which the properties are unknown. However, by making this layer small, its effect on the upper layers (which are of interest here) is negligible.

The Love numbers can be related to the surface values of the y_i's (Jobert, 1973; Tobie et al., 2005),

$$h_2 = y_1|_{r=R_s, \ell=2}, \qquad k_2 = -(y_5|_{r=R_s, \ell=2}) - 1. \tag{A.8}$$

We have benchmarked the propagator matrix solution against the numerical solution by Tobie et al. (2005) for a homogeneous undifferentiated body (Figs. 9a–9d), and for a multi-layered body consisting of an iron core, silicate mantle, and ice shell including a lithosphere layer from Moore and Schubert (2000), both with and without an ocean (Figs. 9e and 9f), and find good agreement with those studies. Fluid layers are approximated as a low-viscosity, low-rigidity viscoelastic material. Rigidity, μ, and viscosity, η have been reduced by a factor of 10^6 and 10^9 respectively, from that of the overlying ice (Table 1). This approximation is valid to within a few percent as long as care is taken that the Maxwell time ($\tau_M = \eta/\mu$) of the fluid layer is not similar to the forcing period, and has been benchmarked against an independent multilayer Love number code (Moore and Schubert, 2000).

Using the same values for the material properties and orbital parameters as Tobie et al. (2005) with our heating formula, we also reproduce the amplitude (0.3 nW m^{-3} globally averaged) and pattern for the heating reported by Tobie et al. (2005) for a homogeneous body.

Appendix B. Symbols used in this work

Although defined in the text, we find it convenient to also present the various symbols used in this paper and their meanings in Table 3.

Table 3
Symbols used in this paper

Symbol	Meaning	Alternate name
A	Pre-exponential viscosity constant	
a, b, c	Primary creep constants	
C	Specific heat	
$\vec{C}$	Vector integration constant	
d	Ice shell thickness	
d_c	Critical ice shell thickness	
E_a	Activation energy	
$\dot{E}_t$	Global dissipation rate	
e	Eccentricity	
$\vec{e}_r$	Unit vector in r direction	
f	Local viscosity perturbation to tidal heating	
F_b	Basal heat flux per unit area	Φ (Tobie et al., 2005)
F_c	Core heat flux per unit area	Φ (Tobie et al., 2005)
G	Gravitational constant	
g	Gravitational acceleration	
H	Volumetric internal heating rate	
H_T	Tidal heating rate per unit volume	
H_{core}	Hent produced in the core rate per unit volume	
h_2	Love number	
I_0	Interface matrix	
i	Inclination	
K	Compressibility or bulk modulus	
k	Thermal conductivity	
k_2	Love number	
k_2^*	Fluid Love number	
ℓ	Spherical harmonic degree	n (Pekeris and Jarosch, 1958; Alterman et al., 1959; Takeuchi et al., 1962; Takeuchi and Saito, 1972)
m	Spherical harmonic order	
N_{20}	Geoid at degree-2	

(*continued on next page*)

Table 3 (*continued*)

Symbol	Meaning	Alternate name
n	Geometric surface-area factor	
P	Pressure	
P_ℓ^m	Associated Legendre function	
Q	Nondimensional load	
R_b	Radius of base of ice shell	
R_c	Core radius	
R_g	Gas constant	
R_s	Surface radius	a (Pekeris and Jarosch, 1958; Alterman et al., 1959; Takeuchi et al., 1962; Takeuchi and Saito, 1972)
Ra	Rayleigh number	
r	Radial position	
s	Length quantity	
T	Temperature	
T_0	Surface temperature	
$T_{0,\mathrm{eq}}$	Surface temperature at equator	
T_b	Basal temperature	
T_T	Tidal period	
t	Time	
$\vec{u}$	Velocity vector	
Y	Propagator matrix	
y_i	Radial functions for spheroidal oscillations	U, V, P (Pekeris and Jarosch, 1958)
α	Coefficient of thermal expansion	
ΔT	Temperature difference across ice shell	
δ_{ij}	Kronecker delta	
$\delta\rho$	Density perturbation	
ε_{ij}	Component of strain in the $i-j$ direction	
$\dot{\varepsilon}_{ij}$	Component of strain rate in the $i-j$ direction	e (Turcotte and Schubert, 2002)
η	Viscosity	
η_0	Basal viscosity	
η_{eff}	Effective viscosity	
η_{ref}	Reference viscosity from tidal heating models, used to normalize f	
η_{sil}	Silicate viscosity	
θ	Co-latitude	
κ	Thermal diffusivity	
λ	Lamé parameter	
μ	Rigidity or shear modulus	G (Turcotte and Schubert, 2002)
$\tilde{\mu}$	Visco-elastic "rigidity"	
ρ	Density	
ρ_0	Reference density	
σ	Stress	
σ_{ij}	Component of stress in the $i-j$ direction	τ_{ij} (Schubert et al., 2000)
τ_M	Maxwell time	
Φ	Tidal potential	
ϕ	Longitude	
ω	Orbital angular frequency	σ (Pekeris and Jarosch, 1958; Alterman et al., 1959)
	Mean motion	n (Murray and Dermott, 1999; Kaula, 1964)

References

Alterman, Z., Jarosch, H., Pekeris, C., 1959. Oscillations of the Earth. Proc. R. Soc. London A 252, 80–95.

Azizi, F., 1989. Primary creep of polycrystalline ice under constant stress. Cold. Reg. Sci. Technol. 16, 159–165.

Barr, A.C., McKinnon, W.B., 2007. Convection in Enceladus' ice shell: Conditions for initiation. Geophys. Res. Lett. 34, doi:10.1029/2006GL028799. L09202.

Biot, M.A., 1954. Theory of stress–strain relationships in anisotropic viscoelasticity and relaxation phenomena. J. Appl. Phys. 25, 1385–1391.

Breuer, D., Yuen, D.A., Spohn, T., 1997. Phase transitions in the martian mantle: Implications for partially layered convection. Earth Planet. Sci. Lett. 148, 457–469.

Collins, G.C., Goodman, J.C., 2007. Enceladus' south polar sea. Icarus 189, 72–82.

Czechowski, L., Leliwa-Kopystyński, J., 2005. Convection driven by tidal and radiogenic heating in medium size icy satellites. Planet. Space Sci. 53, 749–769.

Goldsby, D.L., Kohlstedt, D.L., 2001. Superplastic deformation of ice: Experimental observations. J. Geophys. Res. 106, 11017–11030.

Han, L., Showman, A.P., 2007. Implications of shear heating and fracture zones for ridge formation on Europa. In: Mackwell, S., Stansbery, E. (Eds.), Lunar Planet. Sci. XXXVIII, 2277.

Harder, H., 2000. Mantle convection and the dynamic geoid of Mars. Geophys. Res. Lett. 27, 301–304.

Harder, H., Christensen, U.R., 1996. A one-plume model of martian mantle convection. Nature 380, 507–509.

Jobert, G., 1973. Deformation d'une sphere elastique autogravitante. In: Coulomb, J., Jobert, G. (Eds.), Traite de Geophysiqe intene, 1. Sismologie et pesanteur, vol. 1. Masson, Paris, pp. 171–180.

Kaula, W.M., 1964. Tidal dissipation by solid friction and the resulting orbital evolution. Rev. Geophys. 2, 661–685.

Latychev, K., Mitrovica, J.X., Tromp, J., Tamisiea, M.E., Komatitsch, D., Christara, C.C., 2005. Glacial isostatic adjustment on 3-D Earth models: A finite-volume formulation. Geophys. J. Int. 161, 421–444.

Leliwa-Kopystyński, J., Maruyama, M., Nakajima, T., 2002. The water–ammonia phase diagram up to 300 MPa: Application to icy satellites. Icarus 159, 518–528.

Matson, D.L., Castillo, J.C., Lunine, J., Johnson, T.V., 2007. Enceladus' plume: Compositional evidence for a hot interior. Icarus 187, 569–573.

McKinnon, W.B., 2006. On convection in ice I shells of outer Solar System bodies, with detailed application to Callisto. Icarus 183, 435–450.

McNamara, A.K., Zhong, S., 2005. Degree-one mantle convection: Dependence on internal heating and temperature-dependent rheology. Geophys. Res. Lett. 32, doi:10.1029/2004GL021082. L01301.

Meyer, J., Wisdom, J., 2007. Tidal heating in Enceladus. Icarus 188, 535–539.

Moore, W.B., 2006. Thermal equilibrium in Europa's ice shell. Icarus 180, 141–146.

Moore, W.B., Schubert, G., 2000. Note: The tidal response of Europa. Icarus 147, 317–319.

Multhaup, K., Spohn, T., 2007. Stagnant lid convection in the mid-sized icy satellites of Saturn. Icarus 186, 420–435.

Murray, C.D., Dermott, S.F., 1999. Solar System Dynamics. Cambridge University Press, New York.

Nagel, K., Breuer, D., Spohn, T., 2004. A model for the interior structure, evolution, and differentiation of Callisto. Icarus 169, 402–412.

Nimmo, F., Pappalardo, R.T., 2006. Diapir-induced reorientation of Saturn's Moon Enceladus. Nature 441, 614–616.

Nimmo, F., Spencer, J.R., Pappalardo, R.T., Mullen, M.E., 2007. Shear heating as the origin of the plumes and heat flux on Enceladus. Nature 447, 289–291.

Ojakangas, G.W., Stevenson, D.J., 1989. Thermal state of an ice shell on Europa. Icarus 81, 220–241.

Pekeris, C.L., Jarosch, H., 1958. Free oscillations of the Earth. In: Benioff, H., Ewing, M., Howell Jr., B.F., Press, F. (Eds.), Contributions in Geophysics, vol. 1. Pergamon Press, London, pp. 171–192.

Porco, C.C., Helfenstein, P., Thomas, P.C., Ingersoll, A.P., Wisdom, J., West, R., Neukum, G., Denk, T., Wagner, R., Roatsch, T., Kieffer, S., Turtle, E., McEwen, A., Johnson, T.V., Rathbun, J., Veverka, J., Wilson, D., Perry, J., Spitale, J., Brahic, A., Burns, J.A., DelGenio, A.D., Dones, L., Murray, C.D., Squyres, S., 2006. Cassini observes the active south pole of Enceladus. Science 311, 1393–1401.

Roberts, J.H., Zhong, S., 2004. Plume-induced topography and geoid anomalies and their implications for the Tharsis rise on Mars. J. Geophys. Res. 109, doi:10.1029/2003JE002226. E03009.

Roberts, J.H., Zhong, S., 2006. Degree-1 convection in the martian mantle and the origin of the hemispheric dichotomy. J. Geophys. Res. 111, doi:10.1029/2005JE002668. E06013.

Ross, M.N., Schubert, G., 1986. Tidal dissipation in a viscoelastic planet. J. Geophys. Res. 91, D447–D452.

Ross, M.N., Schubert, G., 1989. Viscoelastic models of tidal heating in Enceladus. Icarus 78, 90–101.

Sabadini, R., Vermeersen, B., 2004. Global Dynamics of the Earth: Applications of Normal Mode Relaxation Theory to Solid-Earth Geophysics. Kluwer Academic Publishers, Dordrecht.

Schubert, G., Turcotte, D.L., Olson, P., 2000. Mantle Convection in the Earth and Planets. Cambridge University Press, Cambridge.

Schubert, G., Anderson, J.D., Travis, B.J., Palguta, J., 2007. Enceladus: Present internal structure and differentiation by early and long-term radiogenic heating. Icarus 188, 345–355.

Scott, T.J., Kohlstedt, D.L., 2004a. The effect of large melt fraction on the deformation behavior of peridotite: Implications for the viscosity of Io's mantle. Lunar Planet. Sci. XXXV. Abstract 1304.

Scott, T.J., Kohlstedt, D.L., 2004b. The effect of large melt fraction on the deformation behavior of peridotite: Implications for the viscosity of Io's mantle and the rheologically critical melt fraction. In: AGU Fall Meeting Abstracts, T13-D02.

Segatz, M., Spohn, T., Ross, M.N., Schubert, G., 1988. Tidal dissipation, surface heat flow, and figure of viscoelastic models of Io. Icarus 75, 187–206.

Sinha, N.K., 1978. Short-term rheology of polycrystalline ice. J. Glaciol. 21, 457–473.

Solomatov, V.S., 1995. Scaling of temperature- and stress-dependent viscosity convection. Phys. Fluids 7, 266–274.

Sotin, C., Head, J.W., Tobie, G., 2002. Europa: Tidal heating of upwelling thermal plumes and the origin of lenticulae and chaos melting. Geophys. Res. Lett. 29, 74-1–74-4.

Spencer, J.R., Pearl, J.C., Segura, M., Flasar, F.M., Mamoutkine, A., Romani, P., Buratti, B.J., Hendrix, A.R., Spilker, L.J., Lopes, R.M.C., 2006. Cassini encounters Enceladus: Background and the discovery of a south polar hot spot. Science 311, 1401–1405.

Squyres, S.W., Reynolds, R.T., Cassen, P.M., 1983. The evolution of Enceladus. Icarus 53, 319–331.

Takeuchi, H., Saito, M., 1972. Seismic surface waves. In: Bolt, B.A. (Ed.), Methods in Computational Physics, vol. 1. Academic Press, New York, pp. 217–295.

Takeuchi, H., Saito, M., Kobayashi, N., 1962. Statical deformations and free oscillations of a model Earth. J. Geophys. Res. 67, 1141–1154.

Tobie, G., Mocquet, A., Sotin, C., 2005. Tidal dissipation within large icy satellites: Applications to Europa and Titan. Icarus 177, 534–549.

Turcotte, D.L., Schubert, G., 2002. Geodynamics, second ed. Cambridge University Press, Cambridge.

Veeder, G.J., Matson, D.L., Johnson, T.V., Davies, A.G., Blaney, D.L., 2004. The polar contribution to the heat flow of Io. Icarus 169, 264–270.

Waite, J.H., Combi, M.R., Ip, W.-H., Cravens, T.E., McNutt, R.L., Kasprzak, W., Yelle, R., Luhmann, J., Niemann, H., Gell, D., Magee, B., Fletcher, G., Lunine, J., Tseng, W.-L., 2006. Cassini Ion and neutral mass spectrometer: Enceladus plume composition and structure. Science 311, 1419–1422.

Willemann, R.J., 1984. Reorientation of planets with elastic lithospheres. Icarus 60, 701–709.

Zhang, S., Christensen, U., 1993. Some effects of lateral viscosity variations on geoid and surface velocities induced by density anomalies in the mantle. Icarus 114, 531–547.

Zhong, S., Zuber, M.T., Moresi, L., Gurnis, M., 2000. Role of temperature-dependent viscosity and surface plates in spherical shell models of mantle convection. J. Geophys. Res. 105, 11063–11082.

Zimmer, C., Khurana, K.K., Kivelson, M.G., 2000. Subsurface oceans on Europa and Callisto: Constraints from Galileo Magnetometer observations. Icarus 147, 329–347.

Zschau, J., 1978. Tidal friction in the solid Earth: Loading tides versus body tides. In: Brosche, P., Suendermann, J. (Eds.), Tidal Friction and the Earth's Rotation. Springer-Verlag, New York, pp. 62–94.